Biochimica et Biophysica Acta 1853 (2015) 2411–2419

Contents lists available at ScienceDirect

Biochimica et Biophysica Acta

journal homepage: www.elsevier.com/locate/bbamcr

Intracellular dynamics and fate of polystyrene nanoparticles in A549 Lung epithelial cells monitored by image (cross-) correlation spectroscopy and single particle tracking

Sarah Deville [a,b], Rozhin Penjweini [a,c], Nick Smisdom [a,b], Kristof Notelaers [a], Inge Nelissen [b], Jef Hooyberghs [b,d], Marcel Ameloot [a,*]

[a] Biomedical Research Unit, Hasselt University, Agoralaan Building C, 3590 Diepenbeek, Belgium
[b] Flemish Institute For Technological Research, Environmental Risk and Health Unit, Boeretang 200, 2400 Mol, Belgium
[c] Department of Radiation Oncology, School of Medicine, University of Pennsylvania, 3400 Civic Boulevard, Philadelphia, PA 19104, USA
[d] Theoretical Physics, Hasselt University, Agoralaan Building D, 3590 Diepenbeek, Belgium

ARTICLE INFO

Article history:
Received 29 March 2015
Received in revised form 19 June 2015
Accepted 7 July 2015
Available online 9 July 2015

Keywords:
Polystyrene nanoparticles
Image correlation spectroscopy
Single particle tracking
Colocalization
Diffusion

ABSTRACT

Novel insights in nanoparticle (NP) uptake routes of cells, their intracellular trafficking and subcellular targeting can be obtained through the investigation of their temporal and spatial behavior. In this work, we present the application of image (cross-) correlation spectroscopy (IC(C)S) and single particle tracking (SPT) to monitor the intracellular dynamics of polystyrene (PS) NPs in the human lung carcinoma A549 cell line. The ensemble kinetic behavior of NPs inside the cell was characterized by temporal and spatiotemporal image correlation spectroscopy (TICS and STICS). Moreover, a more direct interpretation of the diffusion and flow detected in the NP motion was obtained by SPT by monitoring individual NPs. Both techniques demonstrate that the PS NP transport in A549 cells is mainly dependent on microtubule-assisted transport. By applying spatiotemporal image cross-correlation spectroscopy (STICCS), the correlated motions of NPs with the early endosomes, late endosomes and lysosomes are identified. PS NPs were equally distributed among the endolysosomal compartment during the time interval of the experiments. The cotransport of the NPs with the lysosomes is significantly larger compared to the other cell organelles. In the present study we show that the complementarity of ICS-based techniques and SPT enables a consistent elaborate model of the complex behavior of NPs inside biological systems.

1. Introduction

Nanoparticles (NPs) are defined as particles with at least 50% in the number size distribution having one or more external dimensions in the size range between 1 nm and 100 nm [1]. The study of the interaction of NPs with living systems is of steadily growing interest. Since NPs are in the same order of magnitude as biomolecules and viruses, they can easily enter cells and interact with the cellular machinery [2–5]. Although NPs hold great promise for new nanoscaled diagnostics and targeted drug delivery in biological systems [6], they may also provoke toxic side effects [7]. NPs enter cells predominantly through a complex interplay of endocytic pathways and thereafter travel throughout the cell by using its endocytic machinery [8,9]. Primary endocytic vesicles can fuse together with the early endosomes to deliver the cargo for further cellular processing [10]. Early endosomes move towards the perinuclear space, where the transition towards the late endosomes takes place. Finally, the late endosomes fuse with the lysosomes [11]. The intracellular transport of vesicles and cell organelles is mediated through both the microtubules and the actin microfilaments [12]. By studying the trafficking of NPs within living cells and cell organelles, novel insights in NP uptake processes, intracellular transport and their multiple outcomes can be obtained [13].

In the present study, the application of image correlation spectroscopy (ICS) for the determination of interactions of fluorescently stained carboxylated polystyrene (PS) NPs within the cell is presented. PS NPs are commonly used as model NPs to study interaction with biological systems due to their commercial availability, high quality and wide variety of sizes and surface chemistries [8]. ICS is a fluorescence-based microscopic technique suitable for defining the diffusion and directed motion on time scales ranging from microseconds to milliseconds [14–16]. This information is obtained from the fluctuations of the fluorescence intensity within a region of interest (ROI) of a time-lapse image series. Various ICS variants exist which differ in the way how the fluorescence fluctuations in the image series are analyzed. Where in temporal ICS (TICS), fluorescence fluctuations in time for the recorded pixels of an image series are exploited for the correlation analysis [15,17], spatiotemporal ICS (STICS) correlates fluorescence fluctuations

* Corresponding author.
E-mail address: marcel.ameloot@uhasselt.be (M. Ameloot).

http://dx.doi.org/10.1016/j.bbamcr.2015.07.004
0167-4889/

both in space and time [15,18,19]. With these techniques the diffusion and/or flow (magnitude and direction) of molecular complexes can be monitored. They have been used in previous studies to quantify the intracellular transport of the photosensitizer PVP-hypericin, polyplexes, lipoplexes and silica NPs [20–23]. Interaction between molecular complexes is investigated by spatiotemporal image cross-correlation spectroscopy (STICCS) in which space-time correlation functions from the fluorescence intensity fluctuations within a two-channel fluorescence image series are correlated [24]. This approach is used here to study the association of NP complexes with cell organelles. Besides these ensemble averaging techniques, single particle tracking (SPT) can be used to quantify the individual NP motions, which registers and tracks the NP frame by frame [25], as demonstrated for gene nanocarriers and polymeric NPs [26,27].

Here we report on the intracellular dynamics of fluorescently stained carboxylated PS NPs in human alveolar epithelial A549 cells, mimicking the biological responses of lung cells to NP exposure, which is highly relevant for both nanomedicine and nanotoxicology as inhalation is one the major entry routes of NPs to the human body. TICS and STICS were used to characterize the diffusion and map the flow magnitude and direction of PS NPs inside the cell. PS NP motions were also analyzed by SPT, which facilitated in the translation of these general motion models to effective NP dynamics created by biological processes. This was corroborated by dynamic interactions of NPs with the early endosomes, late endosomes and lysosomes established and quantified with STICCS. In addition, the role of cytoskeleton in the NP transport was explored by means of ICS and SPT.

2. Materials and methods

2.1. Cell culture

The human alveolar epithelial A549 cell line was routinely maintained in modified eagle's medium with glutamax (MEM, Gibco, Paisley, United Kingdom) supplemented with 10% non-heat inactivated fetal bovine serum (FBS, Biochrom AG, Berlin, Germany) and 1% penicillin/streptomycin (P/S, Gibco) at 37 °C under 5% CO_2. Before reaching confluence, cells were washed with versene (Gibco) and detached using 0.05% trypsin containing 0.02% EDTA (Sigma-Aldrich, Ayrshire, United Kingdom).

2.2. Nanoparticles

Dark red (λ^{Ex} 660, λ^{Em} 680) fluorescent carboxylated polystyrene nanoparticles (PS NPs) were purchased from Molecular Probes (Invitrogen, Merelbeke, Belgium). PS NPs were characterized by dynamic light scattering (ZetaPALS, Brookhaven Instruments Corporation, Holtsville, USA), yielding a mean hydrodynamic diameter of 116 ± 1 nm (polydispersity index (PDI) of 0.19) in water and 152 ± 2 nm (PDI of 0.18) in complete cell culture medium.

2.3. Cell exposure

The cells used for microscopic observation were plated one day before the experiment in 8 well μ-Slide (Ibidi GmbH, Martinsried, Germany) at a density of 30×10^3 cells/cm^2. Cells were exposed for 30 min to 50 μg/ml of PS NPs diluted in MEM containing 10% FBS, but without phenol red and without P/S at 37 °C under 5% CO_2. After exposure, cells were washed 3 times to remove the PS NPs that were not taken up by the cells and STICS/TICS measurements were conducted. In order to disturb the cytoskeleton mediated transport within the cell, 1 μM latrunculin A (Merck Millipore, Overijse, Belgium) and 20 μM nocodazole (Sigma-Aldrich) were added to the culture medium after NP treatment and washing. After incubation for 30 min, STICS/TICS measurements were performed. For the STICCS measurements, the cells were labeled prior to PS NP exposure with organelle specific dyes. 1 μM LysoTracker® Green DND-26 (Molecular Probes) was added for 30 min. CellLight® Early Endosomes-GFP (Molecular Probes) or CellLight® Late Endosomes-GFP (Molecular Probes) were added to the cultures in a final concentration of 25 particles per cell 24 h prior to the experiments, according to the manufacturer's protocol.

2.4. Immunofluorescence

For visualization of the tubulin and F-actin cytoskeleton, cells exposed to PS NPs, latrunculin A and/or nocodazole were fixed with 4% formalin (Sigma-Aldrich). Cells were permeabilized with 0.5% Tween®20 (Sigma-Aldrich) in PBS for 10 min, and blocked with 0.1% Tween®20 and 2% bovine serum albumin (BSA, Sigma-Aldrich) for 30 min. Subsequently, cells were incubated with mouse anti-tubulin antibodies (T9026, Sigma-Aldrich) for 30 min. After washing the unbound fraction, donkey anti-mouse antibodies conjugated with Alexa Fluor® 488 and CytoPainter Phalloidin-iFluor 555 Reagent (Abcam, Cambridge, UK) were applied for 30 min. Finally, after rinsing the sections extensively, Vectashield® mounting medium containing 4′,6-diamidino-2-phenylindole (DAPI) (Vector Laboratories, Peterborough, United Kingdom) was added.

2.5. Confocal microscopy

Image time-series were acquired using an epifluorescence Axiovert 200 M equipped with a Zeiss LSM 510 Meta confocal laser scanning unit (CLSM, Zeiss, Jena, Germany) and a LD C-Apochromat 40×/1.1 W Korr UV–VIS-IR water immersion objective (Zeiss), placed on a vibration isolation table in an air-conditioned room kept at constant temperature. Cells were kept at 37 °C by the means of a stage incubator (Tempcontrol 37–2 digital, PeCon, Erbach, Germany). Alexa Fluor® 488, CellLight® Early Endosomes-GFP, CellLight® Late Endosomes-GFP and LysoTracker® Green DND-26 were excited with the 488 nm line of an argon ion laser. CytoPainter Phalloidin-iFluor 555 was excited with a 543 nm helium–neon laser. Dark red PS NPs were excited a 633 nm helium–neon laser. DAPI was excited using a 150 fs pulsed laser light of a Ti:Sapphire laser (MaiTai DeepSee, Spectra-Physics, California, USA) tuned at an output wavelength of 730 nm. The excitation light was directed to the sample by a dichroic beam splitter (HFT UV/488/543/633). For the detection and separation of the different emitted fluorescence signals, a secondary dichroic beam splitter NFT 545, as well as four band-pass filters BP 390-465 (DAPI), BP500-550 (Alexa Fluor® 488, CellLight® Early Endosomes-GFP, CellLight® Late Endosomes-GFP, LysoTracker® Green DND-26), BP565-615 (CytoPainter Phalloidin-iFluor 555) or BP650-710 (dark red PS NPs) were used. Signals were directed towards an internal analog photomultiplier tube of the confocal unit. Confocal pinhole was set to a maximum of 1.5 Airy units to provide sufficient z-sectioning. Each image time-series comprised typically 100 frames with a 512 by 512 resolution, a pixel size between 40 and 120 nm, a frame rate of 0.63 Hz without extra time delay between subsequent frames, and a pixel dwell time of 2.51 μs.

2.6. Image (cross-) correlation spectroscopy and colocalization analyses

A brief review of image correlation spectroscopy is given in the Supporting Information. Image (cross-) correlation spectroscopy analysis was performed using custom written MATLAB routines (The MathWorks, Eindhoven, The Netherlands), based on the original work of the Wiseman Research Group (McGill University, Canada). The original routines and details of analysis have been published before [18,19,24,28–31]. Immobile populations within the image series were removed by the means of Fourier-filtering [18]. Due to the flat morphology of the A549 cells, only two-dimensional dynamics were considered.

The central subregion of the spatial autocorrelation of each image in the time series was fit by a two-dimensional Gaussian function yielding the zero-lag amplitude $G(0,0,0)$ and the e^{-2} radius of the point spread function (PSF) of the laser beam ω_0 [18,31]:

$$G(\xi,\eta,0) = G(0,0,0)\ \exp\left\{-\frac{\xi^2+\eta^2}{\omega_0^2}\right\} + G_\infty \quad (1)$$

where ξ and η denote to the spatial lags in x and y directions, respectively, and where G_∞ is the longtime offset.

In TICS, the temporal autocorrelation function, $G(0,0,\tau)$, was fit to the decay models introduced by Hebert et al. for two-dimensional diffusion and/or flow [18]. Among these models, one single species undergoing both diffusion and flow gave the best fit to $G(0,0,\tau)$:

$$G(0,0,\tau) = G(0,0,0)\left(1+\frac{\tau}{\tau_D}\right)^{-1} \times \exp\left\{-\left(\frac{|v_f|\tau}{\omega_0}\right)^2\left(1+\frac{\tau}{\tau_D}\right)^{-1}\right\} + G_\infty \quad (2)$$

where v_f and τ_D refer to the flow velocity and the characteristic diffusion time, respectively.

$\langle\omega_0\rangle$ represents the average of e^{-2} radius of the point spread function (PSF) of the optical setup. The value of $\langle\omega_0\rangle$ was calculated by averaging the individual ω_0 obtained from fitting Eq. (1) for every image in the time series.

The diffusion coefficient (D) was obtained from the characteristic diffusion time, τ_D and $\langle\omega_0\rangle$ according to:

$$D = \frac{\langle\omega_0\rangle^2}{4\tau_D}. \quad (3)$$

For all pairs of images separated by lag-time τ, the spatiotemporal autocorrelation function in STICS is defined by:

$$G(\xi-\Delta\xi,\eta-\Delta\eta,\tau) = G(\Delta\xi,\Delta\eta,\tau)\exp\left\{-\frac{(\xi-\Delta\xi)^2+(\eta-\Delta\eta)^2}{\omega_0(\tau)^2}\right\} + G_\infty. \quad (4)$$

The time-dependent amplitude $G(\Delta\xi, \Delta\eta,\tau)$, the position of the Gaussian peak $(\Delta\xi, \Delta\eta)$ in lag-space and the spatial offset parameter G_∞ were obtained by fitting the experimental data. The displacement of the Gaussian peak over time provides vectorial information about the flow (V_{STICS}) and was always fit to the first linear part detected [18]. The determination of the magnitude of the flow by STICS is more accurate than by TICS [23].

The fitting scheme weights the correlation from each pair of images equally. As photobleaching can affect the primary data [17,32], the autocorrelation function in the presence of photobleaching, $G_{pb}(0,0,\tau)$, was corrected as follows [32]:

$$G_{pb-corrected}(0,0,\tau) = \frac{G_{pb}(0,0,\tau)}{\left\langle[b(t)b(t+\tau)]^{-1/2}\right\rangle_T}, \qquad b(t) = e^{-kt} \quad (5)$$

where $b(t)$ is the time course of particle number concentration during the measurement normalized to the initial concentration; k is the bleaching rate constant with reciprocal time units.

In order to investigate the association between PS NPs and cell organelles, the cross-correlation scheme (STICCS) was employed [18,19,24]. STICCS is based on the image time series in space and time collected in two fluorescence detection channels, *a* from the PS NPs and *b* from labeling of the cell organelle, yielding the cross-correlation function $G_{ab}(\xi,\eta,\tau)$ (see Supporting Information) [15].

The space-time evolution of the cross-correlation function was characterized by locating the maximum of $G_{ab}(\xi,\eta,\tau)$ and fitting with a Gaussian function as presented in Eq. (4). If at zero time-lag the cross-correlation between the two detection channels is non-zero, the two species (PS NPs and organelle specific dye) are in association [18]. However, non-zero cross-correlation values do not automatically imply direct interaction [18]. In the case of stationary particles, the cross-correlation stays unchanged for all values of τ and centers at $(\xi = 0, \eta = 0)$. Changes over time in the number of interacting and/or correlating particles that are at the same location in space will be reflected in the cross-correlation function as described for STICS.

From the recorded confocal time-lapse movies image subsections of 64×64 pixels in size were selected from different regions in the cell for STICS, TICS and STICCS analyses. Median values were taken from at least 10 regions inside the cell as an estimate for the average motion per cell. For STICCS, the absence of cross-talk between the fluorescently labeled cell organelles and the NPs was verified.

Stage drift was assessed by performing the STICS analysis to fixed beads (Invitrogen, PS-Speck Microscope Point Source Kit, nominal diameter 175 nm) mounted on a coverslip under the same environment and set-up as in the actual experiments. The magnitude of the stage drift was about $(1.5 \pm 0.1) \times 10^{-3}$ μm/s. STICS analysis was performed on the entire image (512×512 pixels) giving an estimate of the experimental cell motions and stage drift. Velocities obtained from individual regions within cells were corrected accordingly.

Colocalization analyses of nanoparticles with organelles was also performed by calculating the Manders' overlap coefficients M1 and M2 by using the JACoP plugin in ImageJ (National Institutes of Health, Bethesda, United States) [33,34]. Prior to the colocalization analysis, the threshold was set to the estimated value of the background. Subsequently, the M1 and M2 colocalization coefficients were defined by Eqs. (6)–(7) with A_i and B_i the signal intensity above a selected threshold of pixel number i obtained from the channel representing respectively the organelle type and nanoparticles:

$$M_1 = \frac{\sum_i A_{i,coloc}}{\sum_i A_i} \quad (6)$$

where $A_{i,coloc} = A_i$ if $B_i > 0$ and $A_{i,coloc} = 0$ if $B_i = 0$ and

$$M_2 = \frac{\sum_i B_{i,coloc}}{\sum_i B_i} \quad (7)$$

where $B_{i,coloc} = B_i$ if $A_i > 0$ and $B_{i,coloc} = 0$ if $A_i = 0$. Obtained overlap coefficients are not dependent on the relative intensities of each channel [33]. Cross-talk between the double labeled cells was found to be negligible.

2.7. Single particle tracking

SPT analysis was performed on the same experimental data of PS NPs as used for ICS analysis. Particles were localized in each frame by automated tresholding and Gaussian fitting [35]. Trajectories were constructed by connecting particle locations in subsequent frames, while minimizing the total square displacement [36]. For all trajectories, containing at least 12 displacements, the mean square displacement (MSD) $\langle r^2\rangle$ was determined over all pairs of points for the available time lags. Each trajectory provided an estimator of the diffusion coefficient D_{est} by linear least squares fitting of the MSD in function of the first three time lags (t_{1-3}) according to 2D Brownian motion:

$$\langle r^2\rangle = 4D_{est}t_{1-3} \quad (8)$$

Particle trajectories not displaying an increase in MSD over increasing time lags were considered to be *immobile* (I) and the corresponding values were excluded from the distribution of D_{est}. Segments of directed motion were identified in particle trajectories by a scanning window analysis [37]. Elongated trajectory sections were identified based on the radius of gyration and identified as directed motion if the net

displacement (R) was sufficient according to:

$$R > \sqrt{4D_e t} \quad (9)$$

where D_e represents the diffusion coefficient D_{est} averaged over all trajectories of the non-treated, control condition ($0.011 \pm 0.001\ \mu m^2/s$) and t is the *duration* of the time section. The *distance* of the section was quantified as the scalar sum of all first order displacements within t. The *speed* was obtained by dividing the *distance* by *duration*. All image processing and consequent analyses were performed by in-house developed MATLAB routines.

2.8. Statistical analysis

Statistical analyses were performed by GraphPad Prism version 5.00 (GraphPad Software, San Diego, California, USA). Student's t-tests were performed in order to investigate the effect of nocodazole and latrunculin A on the flow and diffusion values obtained from STICS, TICS and SPT. A Kruskal–Wallis test was performed to compare the correlated motion velocities of PS NPs with the cell organelles. Results with p-values smaller than 0.05 were considered to be statistically significant.

3. Results and discussion

3.1. Nanoparticle dynamics within cytosol

PS NPs can enter A549 cells through multiple endocytic pathways [8,9,38]. The subsequent phenomena of non-directed and possible directed motion of PS NPs within the cytosol of A549 was investigated by STICS and TICS. Fig. 1 displays for a typical cellular region (region 1 from Fig. 2a) the STICS spatiotemporal autocorrelation function (STACF) at $\tau = 0$, 20 and 40 s (Fig. 1a), the time evolution of its peak position (Fig. 1b) and the TICS temporal autocorrelation function (TACF) (Fig. 1c). Fitting for the displacement of the Gaussian peak yielded the velocity $V_{STICS} = 7.4 \times 10^{-3}\ \mu m/s$ ($v_\xi = 6.2 \times 10^{-3}\ \mu m/s$; $v_\eta = 4.1 \times 10^{-3}\ \mu m/s$) (Fig. 1b, using only the linear part of the traces). Fitting the TACF with a model for diffusion and flow yields the diffusion coefficient $D_{TICS} = 0.8 \times 10^{-3}\ \mu m^2/s$ when the flow magnitude was fixed at the obtained value for V_{STICS} (Fig. 1c). The same STICS and TICS analyses were executed for the different regions inside the cell (Fig. 2, Table S1). The velocity mapping shows locally directed motion of different magnitudes for intracellular NP transport, where the median of the flow and diffusion values inside the cell equal to V_{STICS} ($N = 1$) = $9.9 \times 10^{-3}\ \mu m/s$ and D_{TICS} ($N = 1$) = $18.5 \times 10^{-3}\ \mu m^2/s$. Values obtained from different biological cells ($N = 5$) were averaged over the median of each cell, resulting in V_{STICS} ($N = 5$) = $(9 \pm 2) \times 10^{-3}\ \mu m/s$ and D_{TICS} ($N = 5$) = $(8 \pm 3) \times 10^{-3}\ \mu m^2/s$ (average ± SEM); Table 1). These values are in close agreement with the velocity and diffusion acquired from polyplexes in CHO-K1 cells studied with STICS [22]. In contrast, the values are respectively 10 times and 5 times smaller than the results obtained with STICS for SiO_2 NPs in A549 cells and polyplexes in HeLa [20,21]. Little is known about the influence of NP exposure on the regulation of the endocytic pathways and the speed of vesicle trafficking. For that reason, the divergence can possibly be attributed to the differences in exposure time, the type of NP or their uptake pathways.

The intracellular transport of vesicles and cell organelles is mediated through both the microtubules and the actin microfilaments [12]. In order to explore the role of these cytoskeleton assemblies in PS NP dynamics, nocodazole and latrunculin A were added to the cultures after NP internalization. Nocodazole and latrunculin A interfere with the polymerization of the tubulin and actin cytoskeleton respectively, significantly reducing the transport that they mediate [21,39]. Effectivity of nocodazole and latrunculin A inhibition was verified by means of immunofluorescence (Fig. S1). Flow velocities and diffusion values from 5 independent cells were compared to evaluate the effects of nocodazole and latrunculin A (Fig. 2, Table 1). Nocodazole treatment

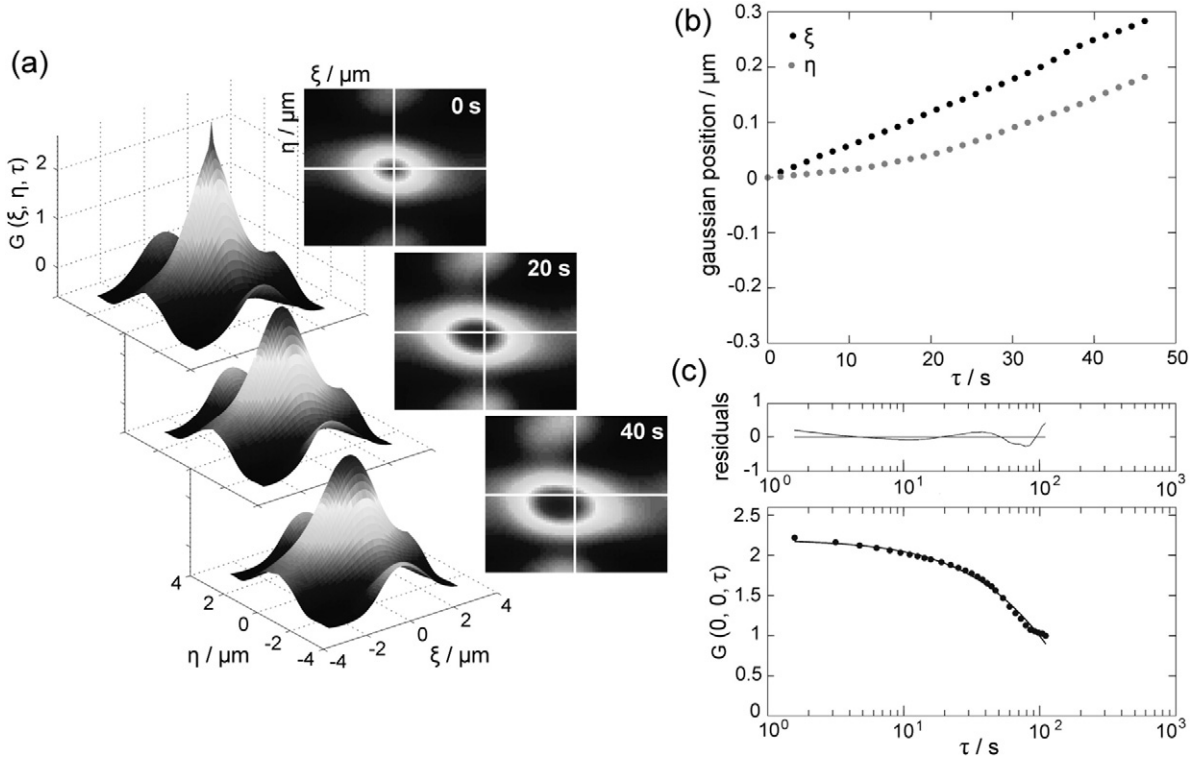

Fig. 1. STICS and TICS analyses of PS NPs in A549 cells. Image subsections of 64 × 64 pixels were selected from different regions of the cells shown in Fig. 2a. Here region 1 is presented. (a) Spatiotemporal autocorrelation functions $G(\xi,\eta,\tau)$ (STACF) and their contour plot at different time points. (b) Time dependence of the position of the peak of the STACF. (c) The temporal autocorrelation function $G(0,0,\tau)$ (TACF) was fitted using a diffusion model, considering a fixed flow component as determined by STICS.

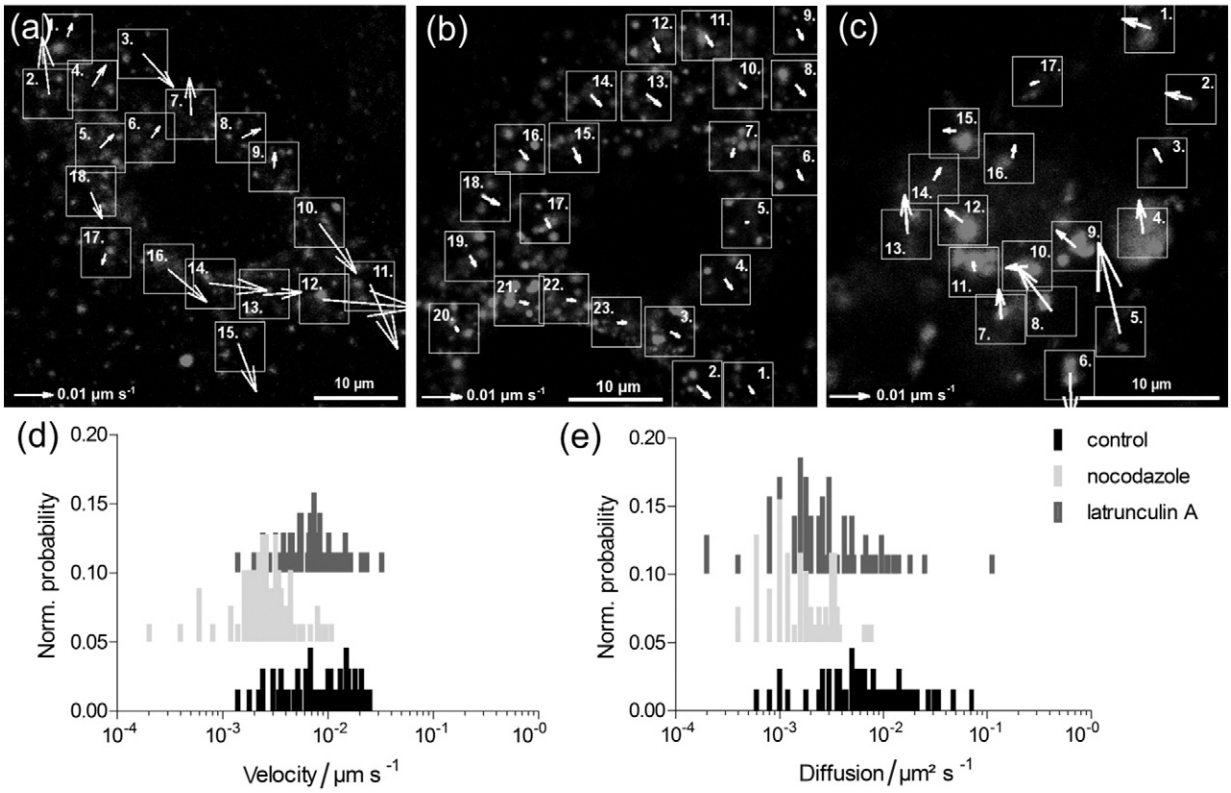

Fig. 2. The role of the cytoskeleton in the intracellular dynamics of PS NP transport within A549 cells based on STICS and TICS analyses. Velocity mapping of NP dynamics without treatment (a), and after treatment with 20 μM nocodazole (b) and 500 nM latrunculin A (c). Flow velocities and diffusion coefficients of the presented cells are shown in Table S1. (d–e) Frequency distribution histograms of NP velocity and diffusion coefficient from ROIs of 5 independent cells (expressed as the normalized probability) without (control) and after treatment with cytoskeletal inhibitors.

dramatically reduced the motion of the PS NPs when compared to the untreated cells. The flow velocity dropped significantly from $(9 \pm 2) \times 10^{-3}$ μm/s to $(2.7 \pm 0.2) \times 10^{-3}$ μm/s ($p = 0.0141$), whereas the diffusion coefficient decreased significantly from $(8 \pm 3) \times 10^{-3}$ μm²/s to $(1.3 \pm 0.3) \times 10^{-3}$ μm²/s (p-value = 0.029). In contrast, latrunculin A treatment did not affect the velocity ($(8 \pm 2) \times 10^{-3}$ μm/s). The diffusion coefficient was reduced ($(2 \pm 1) \times 10^{-3}$ μm²/s), although this reduction is not significant ($p = 0.0543$). These findings suggest that the microtubules play a key role in mediating the directed transport of the PS NPs within the cell. Moreover, it indicates that the obtained velocity from STICS represents the activity of the microtubule motors when the PS NPs are transported through the cell [40]. In accordance with our findings, nocodazole treatment of cells exposed to quantum dots and polyplexes was shown to abolish the microtubule associated active transport [21,41,42], while prevention of the F-actin cytoskeleton polymerization with cytochalasin D did not interfere with the active transport [41].

In order to pursue a more direct interpretation of the diffusion and flow detected in the NP motion, SPT was applied on the same data sets (Fig. 3). NPs were traced and these traces were analyzed for diffusion and directed motion. Analysis of the mean square displacements (MSDs) reveals a broad distribution of diffusion coefficient estimators, spanning four orders of magnitude (Fig. 3e), which is analogous to the distribution of the diffusion coefficient estimators obtained by TICS (Fig. 2e). This finding suggests anomalous diffusion and/or multiple diffusion modes [43]. Furthermore, compared to the control, the distribution of the diffusion coefficient estimators shows a slight shift for latrunculin A and a large shift for nocodazole treatment towards lower values. This is also reflected in the average diffusion coefficient estimators: control $(11 \pm 1) \times 10^{-3}$ μm²/s, nocodazole $(2.7 \pm 0.2) \times 10^{-3}$ μm²/s and latrunculin A $(7.0 \pm 0.5) \times 10^{-3}$ μm²/s, yielding a significant difference between control and nocodazole ($p = 0.002$) (Table 2). These diffusion coefficients are in the same order of magnitude as the mean values of TICS. However, diffusion is considered to be a thermal process and should thereby be independent of treatment conditions [44–46]. The results of TICS and SPT therefore suggest that the random walk-like behavior of the NPs is part of an active cellular capture process linked to microtubules and can be attributed to diffusive interphases present in the directed transport. This phenomenon has been described before for the cytoskeletal transport of early endosomes [47,48]. Disruption of the cytoskeleton can, consequently, impair track switching and therefore contribute to a change in the PS NP apparent diffusion.

The presence of directed motion supports the notion of cellular control over intracellular particle dynamics. Using trajectory analysis, sections of directed motion could be identified in the particle traces (Fig. 3a-c). Direct investigation of the trajectories shows that particles often display saltatory motion without any overall directionality [49]. Consistent analysis of all conditions shows that this motion type occurs frequently in control conditions 38 ± 4%, but is strongly abolished under influence of nocodazole 9 ± 1% (p-value < 0.0001) (Table 2). The approximate range of the SPT-measured directed motion speed

Table 1
Parameters of NP motions extracted by STICS and TICS analysis. Reported values are averaged over the median of the parameter values obtained for the different regions of each cell ($N = 5$) and represented with standard error. The asterisk denotes significant differences of treatment compared to control conditions (*p-value < 0.05).

Motion type	A549 cell treatment		
	Control	Nocodazole	Latrunculin A
Diffusion [μm²/s]	$(8 \pm 3) \times 10^{-3}$	$(1.3 \pm 0.3) \times 10^{-3*}$	$(2 \pm 1) \times 10^{-3}$
Velocity [μm/s]	$(9 \pm 2) \times 10^{-3}$	$(2.7 \pm 0.2) \times 10^{-3*}$	$(8 \pm 2) \times 10^{-3}$

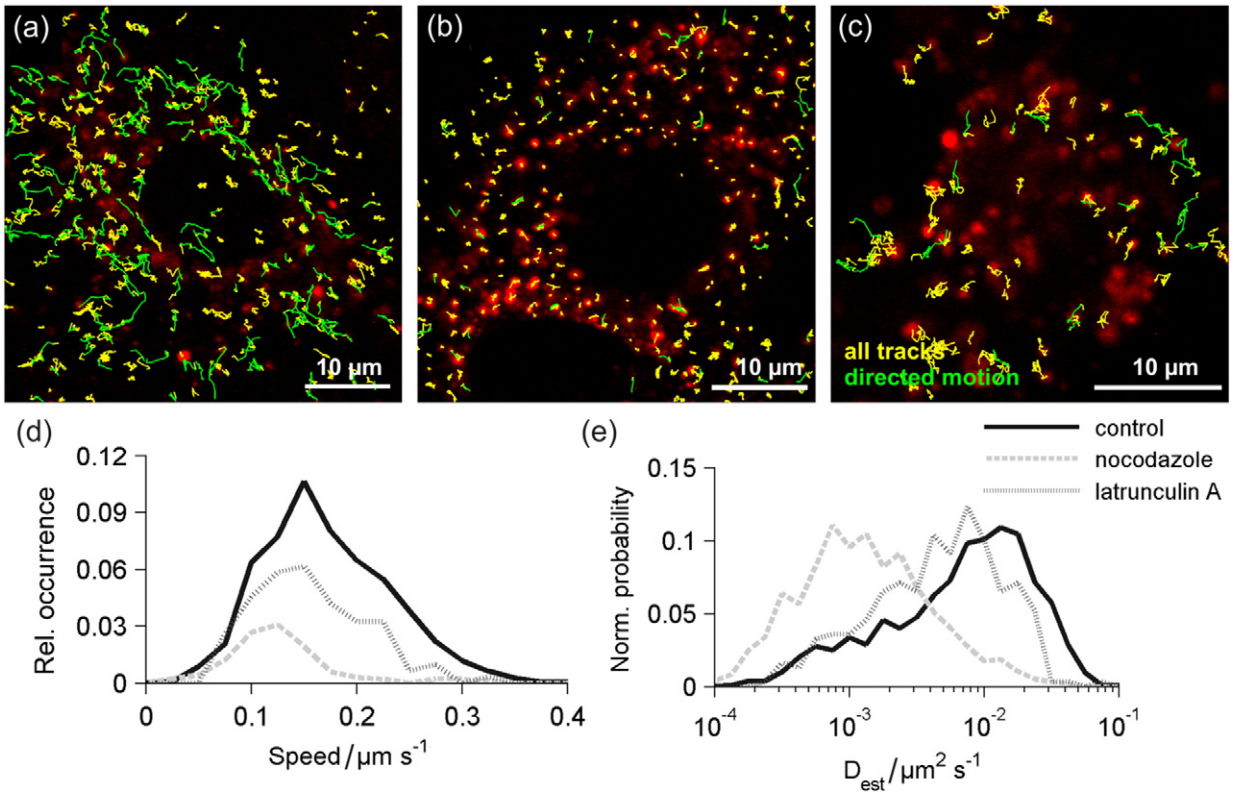

Fig. 3. Tracking and quantification of PS NP intracellular dynamics and the role of the cytoskeleton in A549 cells using SPT analysis. (a–c) All PS NP identified tracks (yellow), the identified directed motion sections (green) and PS NPs (red) in cells without treatment (a), or treated with 20 μM nocodazole (b) and 500 nM latrunculin A (c) are displayed. The first image of the time series is presented. (d) The distribution of the speed of NP transport over the sections is shown per treatment. The area under the curve represents the relative contribution of directed motion to the overall PS NP dynamics in each condition. (e) From each trajectory an estimator of the diffusion coefficient (D_{est}) was determined and the corresponding distribution over all trajectories from each treatment is shown. The normalization is with respect to the total number of trajectories in each condition.

(0.1 μm/s to 0.3 μm/s) under control conditions (Fig. 3d) is overlapping with results of microtubule-assisted transport speeds of organelles and NPs reported in the literature [40,42,50]. Also, values between 0.2 μm/s and 1.5 μm/s have been reported for the active intracellular transport of quantum dots in A549 cells [42]. The *speed* and *distance* of the remaining directed motion under nocodazole conditions is also significantly decreased compared to the control, 0.127 ± 0.005 μm/s vs 0.169 ± 0.007 μm/s ($p = 0.0013$) and 1.9 ± 0.2 μm vs 2.71 ± 0.08 μm ($p = 0.0011$), suggesting less efficient NP transport (Table 2). Under latrunculin A influence, the directed motion of the NPs mainly seems to vary as a consequence of cell morphology changes (Fig. 3c). This is corroborated by the directed motion *distance* being the only significantly decreased parameter under latrunculin A treatment compared to control, 2.0 ± 0.2 μm vs 2.71 ± 0.08 μm ($p = 0.0082$). Latrunculin A induced cell shrinking can be expected to reduce NP transport distance [51].

3.2. Colocalization of polystyrene nanoparticles with cell organelles

In order to investigate the accumulation and transport of PS NPs within the early endosomes, late endosomes and lysosomes, the fluorescent signals of the PS NPs were correlated with the signals of, respectively, Early Endosomes-GFP, Late Endosomes-GFP and LysoTracker® Green DND-26. The distribution and localization of PS NPs within the endolysosomal compartment was investigated by static colocalization analyses using Manders' overlap coefficients (Table 3, Fig. S2). The Manders' overlap coefficients M1 and M2 describe the colocalization of PS NPs with the cell organelle of interest [33]. M1 represents the fraction of the labeled organelle containing PS NPs, whereas M2 represents the fraction of PS NPs associated with the labeled organelle. PS NPs were almost equally distributed among the early endosomes (18 ± 2%), late endosomes (28 ± 3%) and lysosomes (20 ± 3%) during the time interval of the experiments.

Table 2
Parameters of NP motion extracted by SPT analysis. Diffusion parameters were determined by analyzing the MSD in function of time using a linear model (Eq. (8)). Sections of directed motion were also extracted from the trajectories and individually quantified. Values reported here are averaged over mean parameter values of each cell ($N = 5$) and represented with standard error. The asterisk denotes significant differences of treatment compared to control conditions (**p-value < 0.01).

Motion type	Parameter	A549 cell treatment		
		Control	Nocodazole	Latrunculin A
Diffusion	D_{est} [μm²/s][a]	$(11 \pm 1) \times 10^{-3}$	$(2.7 \pm 0.2) \times 10^{-3}$ **	$(7.0 \pm 0.5) \times 10^{-3}$
	I [%][b]	8 ± 2	7 ± 1	4 ± 1
Directed motion	prevalence [%]	38 ± 4	9 ± 1**	25 ± 3
	duration [s]	16.4 ± 0.6	15 ± 1	13.4 ± 0.8
	distance [μm]	2.71 ± 0.08	1.9 ± 0.2**	2.0 ± 0.2**
	speed [μm/s]	$(169 \pm 7) \times 10^{-3}$	$(127 \pm 5) \times 10^{-3}$**	$(150 \pm 10) \times 10^{-3}$

[a] Estimated diffusion coefficient by linear least squares fitting of the MSD.
[b] Immobile fraction.

Table 3
Distribution of PS NPs within early endosomes, late endosomes and lysosomes using Manders' overlap coefficients, together with the standard error of the mean over *N* cells. M1 represents the fraction of labeled organelle colocalizing with the PS NPs, whereas M2 represents the fraction of PS NPs colocalizing with the labeled organelle.

	M1	M2	*N*
Early endosomes	0.15 ± 0.01	0.18 ± 0.02	29
Late endosomes	0.16 ± 0.02	0.28 ± 0.03	21
Lysosomes	0.12 ± 0.02	0.20 ± 0.03	18

Conventional static dual-color colocalization imaging has been applied before to study the accumulation of NPs in specific cell organelles [16,20,21]. Quantitative analysis often suffers from intrinsic user bias in defining an intensity threshold. STICCS overcomes the limitations of conventional colocalization analyses by analyzing the correlated motion of NPs and cellular organelles. Therefore, the kinetics of potentially correlated motions (dynamic colocalization) of NPs within the endosomes and lysosomes were further explored by STICCS. Although STICCS reveals comigrating complexes, it has to be noted however that this does not indicate whether they are necessarily in direct contact [24]. For each cell organelle type, a typical STICCS analysis is presented in Fig. 4 with an image from the time-series, the contour plot of the Gaussian cross-correlation peak $G(\xi,\eta,\tau)$ for $\tau = 0$, 20 and 40 s, the position of $G(\xi,\eta,\tau)$ peak as a function of time, and the velocity mapping of the cotransport inside the whole cell (values are given in Table S2). The Gaussian cross-correlation peak $G(\xi,\eta,\tau)$ for both endosomes and lysosomes is very strong, indicating that correlated motions between the PS NPs and these cell organelles were detected. The peak appears to be mobile as a function of time and broadens by increasing time lags, indicating that the mobile population of PS NPs cotransported with the organelles exhibits a combination of directed movement interspersed with diffusive pauses. Fitting the displacement of $G(\xi,\eta,\tau)$ yields directional flow information of the colocalized PS NPs and the cell organelle of interest (Fig. 4b–c). The STICCS analyses results show an asymmetric peak, which could be attributed to the spatial distribution of the PS NPs and/or the asymmetric shape of the cell organelles. STICCS analyses of the complete A549 cell, considering 512 × 512 pixels, labeled with the organelle specific dye and the fluorescently labeled PS NPs were performed. Lysosomes had a significantly higher cotransport velocity ($(212 \pm 45) \times 10^{-3}$ μm/s, N = 18) compared to early endosomes ($(52 \pm 9) \times 10^{-3}$ μm/s, N = 15) and late endosomes ($(35 \pm 7) \times 10^{-3}$ μm/s, N = 15) ($p < 0.0001$). STICS analyses on the organelle population were performed as well in cells which were exposed to PS NPs. Early endosomes presented $V_{STICS} = (6 \pm$

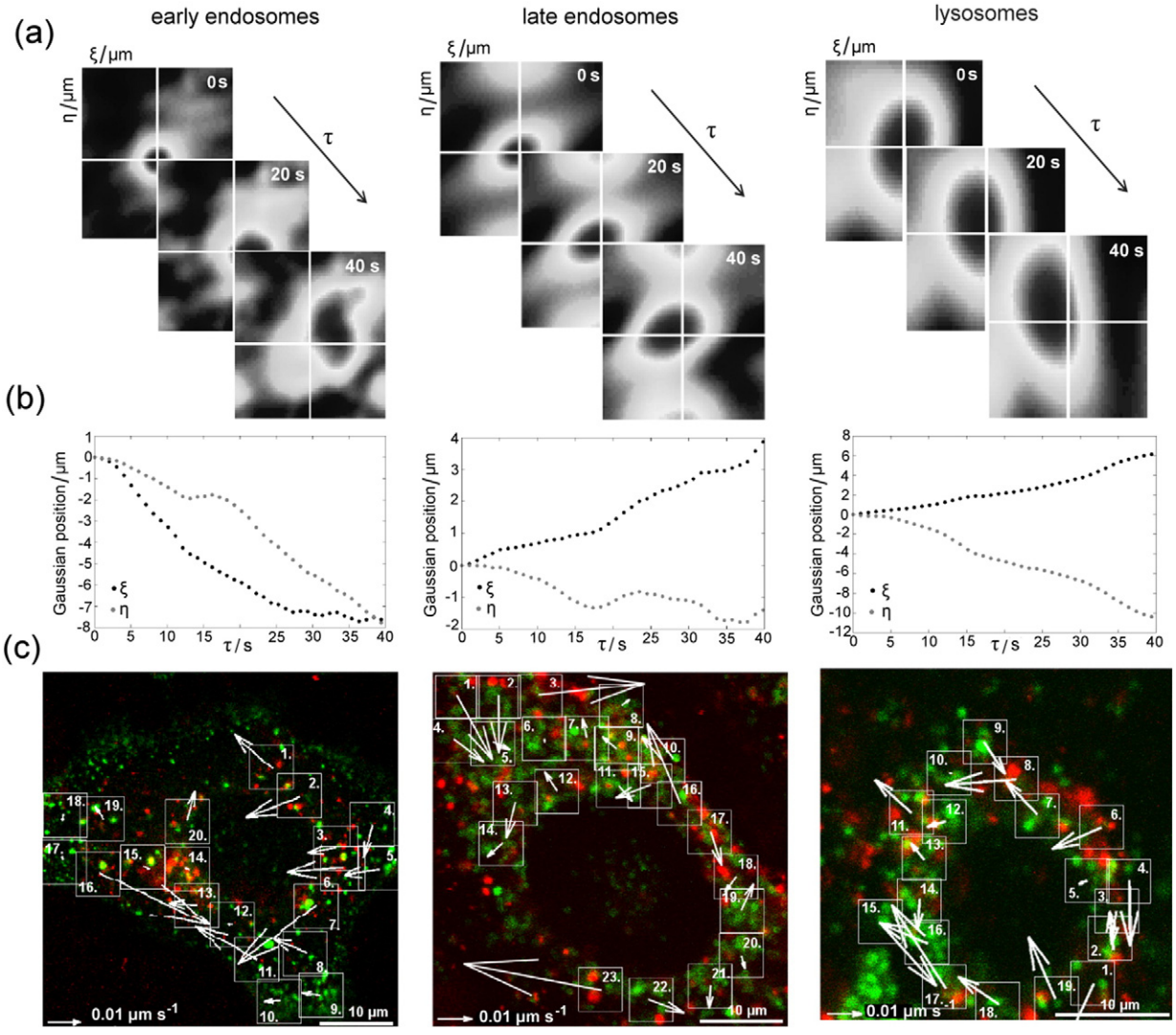

Fig. 4. STICCS analyses of correlated motions of PS NPs with early endosomes, late endosomes and lysosomes within A549 cells. (a) Contour plot of the cross-correlation peak $G(\xi,\eta,\tau)$ for $\tau = 0$, 20 or 40 s for early endosomes (ROI 16), late endosomes (ROI 17) and lysosomes (ROI 1). (b) Position of $G(\xi,\eta,\tau)$ as a function of τ. (c) Dual-channel time series image with PS NPs (in red) and cell organelle (in green) together with velocity mapping of NP correlated motions (Fig. S2). Effective flow velocities of the cotransport in all ROIs (numbered boxes) are presented Table S2.

2) $\times 10^{-3}$ μm/s), late endosomes $V_{STICS} = (4 \pm 1) \times 10^{-3}$ μm/s) and lysosomes $V_{STICS} = (5 \pm 1) \times 10^{-3}$ μm/s). Compared to literature, the acquired velocities for the PS NP cotransport with the endosomal transport resemble the average velocity of the early endosomes (approximately 12×10^{-3} μm/s) [52]. On the contrary, others report velocities of early endosomes between approximately 400–800 $\times 10^{-3}$ μm/s [53]. Vesicle speed of late endosomes was reported approximately 250×10^{-3} μm/s [54]. The velocities obtained for the PS NP cotransport with the lysosomes are in close approximation to the reported active transport velocities of the lysosomes approximately 200–700 $\times 10^{-3}$ μm/s [55–57].

Correlated flow velocities of PS NPs together with cell organelles obtained by STICCS are remarkably higher than the velocities obtained for PS NPs and cell organelles with STICS. Similar effects have been observed with biodegradable poly L-lactic acid nanocarriers (~200 nm size) also in A549 cells (unpublished data). STICS provides the most accurate information on transport dynamics if the process exhibits a unidirectional flow pattern which can be averaged over a sufficient number of particles [18]. If, on the other hand, the organelle mediated transport is not unidirectional, the averaged velocity determined by STICS will underestimate the actual transport velocities. Furthermore, if only the PS NPs associated with the organelles of interest are considered, as achieved through cross-correlation, the averaging effect is reduced. This results in more representative values of the velocity. These values as obtained by STICCS resemble those as recovered by SPT when analyzing individual tracks of PS NPs. Therefore, both STICCS and SPT provide reliable information on specific organelle mediated transport of PS NPs. Despite the averaging effect in STICS, both STICS and SPT indicate diminished PS NP dynamics upon nocodazole treatment. This demonstrates the significance of the microtubule cytoskeleton in PS NP transport.

4. Conclusion

Various aspects of the trafficking of NPs inside the cells remain largely unknown. Measuring their intracellular dynamics is considered as a fundamental step in understanding their complex behavior. In this work, we presented the application of ICS-based techniques and SPT to characterize the directed motion and diffusion characteristics of internalized PS NPs in A549 lung cells. We applied TICS and STICS to characterize the diffusion, and map the flow magnitude and direction of PS NPs inside the cell. STICS and TICS analyses were shown to be a powerful tool for determining the ensemble kinetic behavior of NPs inside the cell. Moreover, when NPs are not clearly resolved, the employed techniques can reveal information concerning their intracellular movement. In addition, SPT was used in order to retrieve a more direct interpretation of the diffusion and flow detected in NP motion by defining the trajectories of NPs. STICS and SPT in combination with cytoskeleton inhibitors revealed that PS NP directed motions were strongly dependent on microtubule-assisted transport. Moreover, by applying STICCS, we were able to detect the correlated motions of PS NPs with the early endosomes, late endosomes and lysosomes. Both SPT and STICCS provided information on specific organelle mediated transport of PS NPs in A549 cells. In summary, the combination of ICS-based techniques and SPT can obtain novel insights into the complex behavior of NPs inside biological systems and represents a valuable tool for both nanosafety assessment and nanomedicine.

Transparency document

The Transparency document associated with this article can be found, in the online version.

Acknowledgments

The authors would like to acknowledge funding from INTERREG-IV A (BioMiMedics), BOF (Hasselt University) and a tUL impulse grant Phase II by the Province of Limburg (Belgium). NS was supported by a post-doctoral scholarship of Research Foundation Flanders (FWO-Vlaanderen).

Appendix A. Supplementary data

Supplementary data to this article can be found online at http://dx.doi.org/10.1016/j.bbamcr.2015.07.004.

References

[1] Commision recommendation of 18 October 2011 on the definition of nanomaterial (2011/696/EU), Off. J. Eur. Union (2011) 38–40.
[2] J.A. Kim, C. Aberg, G. de Carcer, M. Malumbres, A. Salvati, K.A. Dawson, Low dose of amino-modified nanoparticles induces cell cycle arrest, ACS Nano 7 (9) (2013) 7483–7494.
[3] A. Salvati, C. Åberg, T. dos Santos, J. Varela, P. Pinto, I. Lynch, K.A. Dawson, Experimental and theoretical comparison of intracellular import of polymeric nanoparticles and small molecules: toward models of uptake kinetics, Nanomed. Nanotechnol. Biol. Med. 7 (2011) 818–826.
[4] J. Rejman, V. Oberle, I.S. Zuhorn, D. Hoekstra, Size-dependent internalization of particles via the pathways of clathrin- and caveolae-mediated endocytosis, Biochem. J. 377 (2004) 159–169.
[5] B.D. Chithrani, A.A. Ghazani, W.C. Chan, Determining the size and shape dependence of gold nanoparticle uptake into mammalian cells, Nano Lett. 6 (2006) 662–668.
[6] I. Ojea-Jimenez, J. Comenge, L. Garcia-Fernandez, Z.A. Megson, E. Casals, V.F. Puntes, Engineered inorganic nanoparticles for drug delivery applications, Curr. Drug Metab. 14 (2013) 518–530.
[7] J. Boczkowski, P. Hoet, What's new in nanotoxicology? Implications for public health from a brief review of the 2008 literature, Nanotoxicology 4 (2010) 1–14.
[8] J.A. Varela, M.G. Bexiga, C. Aberg, J.C. Simpson, K.A. Dawson, Quantifying size-dependent interactions between fluorescently labeled polystyrene nanoparticles and mammalian cells, J. Nanobiotechnol. 10 (2012) 39.
[9] T. dos Santos, J. Varela, I. Lynch, A. Salvati, K.A. Dawson, Effects of transport inhibitors on the cellular uptake of carboxylated polystyrene nanoparticles in different cell lines, PLoS One 6 (2011) e24438.
[10] S. Mayor, R.E. Pagano, Pathways of clathrin-independent endocytosis, Nat. Rev. Mol. Cell Biol. 8 (2007) 603–612.
[11] E. Frohlich, C. Meindl, E. Roblegg, B. Ebner, M. Absenger, T.R. Pieber, Action of polystyrene nanoparticles of different sizes on lysosomal function and integrity, Part. Fibre Toxicol. 9 (2012) 26.
[12] T. Soldati, M. Schliwa, Powering membrane traffic in endocytosis and recycling, Nat. Rev. Mol. Cell Biol. 7 (2006) 897–908.
[13] A. Panariti, G. Miserocchi, I. Rivolta, The effect of nanoparticle uptake on cellular behavior: disrupting or enabling functions? Nanotechnol. Sci. Appl. 5 (2012) 87–100.
[14] N.O. Petersen, P.L. Hoddelius, P.W. Wiseman, O. Seger, K.E. Magnusson, Quantitation of membrane receptor distributions by image correlation spectroscopy: concept and application, Biophys. J. 65 (1993) 1135–1146.
[15] P.W. Wiseman, Chapter ten — image correlation spectroscopy: mapping correlations in space, time, and reciprocal space, in: Y.T. Sergey (Ed.), Methods in Enzymology, Academic Press 2013, pp. 245–267 (Place Published).
[16] P.W. Wiseman, N.O. Petersen, Image correlation spectroscopy. II. Optimization for ultrasensitive detection of preexisting platelet-derived growth factor-beta receptor oligomers on intact cells, Biophys. J. 76 (1999) 963–977.
[17] D.L. Kolin, S. Costantino, P.W. Wiseman, Sampling effects, noise, and photobleaching in temporal image correlation spectroscopy, Biophys. J. 90 (2006) 628–639.
[18] B. Hebert, S. Costantino, P.W. Wiseman, Spatiotemporal image correlation spectroscopy (STICS) theory, verification, and application to protein velocity mapping in living CHO cells, Biophys. J. 88 (2005) 3601–3614.
[19] M. Rossow, W.W. Mantulin, E. Gratton, Spatiotemporal image correlation spectroscopy measurements of flow demonstrated in microfluidic channels, J. Biomed. Opt. 14 (2009) 024014.
[20] C. Schumann, S. Schubbe, C. Cavelius, A. Kraegeloh, A correlative approach at characterizing nanoparticle mobility and interactions after cellular uptake, J. Biophotonics 5 (2012) 117–127.
[21] R.P. Kulkarni, D.D. Wu, M.E. Davis, S.E. Fraser, Quantitating intracellular transport of polyplexes by spatio-temporal image correlation spectroscopy, Proc. Natl. Acad. Sci. U. S. A. 102 (2005) 7523–7528.
[22] S. Coppola, D. Pozzi, S.C. De Sanctis, M.A. Digman, E. Gratton, G. Caracciolo, Quantitative measurement of intracellular transport of nanocarriers by spatio-temporal image correlation spectroscopy, Methods Appl. Fluoresc. 1 (2013).
[23] R. Penjweini, N. Smisdom, S. Deville, M. Ameloot, Transport and accumulation of PVP-Hypericin in cancer and normal cells characterized by image correlation spectroscopy techniques, Biochim. Biophys. Acta, Mol. Cell Res. 1843 (2014) 855–865.
[24] T. Toplak, E. Pandzic, L. Chen, M. Vicente-Manzanares, A.R. Horwitz, P.W. Wiseman, STICCS reveals matrix-dependent adhesion slipping and gripping in migrating cells, Biophys. J. 103 (2012) 1672–1682.
[25] E. Zagato, K. Forier, T. Martens, K. Neyts, J. Demeester, S. De Smedt, K. Remaut, K. Braeckmans, Single-particle tracking for studying nanomaterial dynamics: applications and fundamentals in drug delivery, Nanomedicine (Lond.) 9 (2014) 913–927.
[26] J. Suh, D. Wirtz, J. Hanes, Real-time intracellular transport of gene nanocarriers studied by multiple particle tracking, Biotechnol. Prog. 20 (2004) 598–602.

[27] S.K. Lai, K. Hida, C. Chen, J. Hanes, Characterization of the intracellular dynamics of a non-degradative pathway accessed by polymer nanoparticles, J. Control. Release 125 (2008) 107–111.
[28] J. Bove, B. Vaillancourt, J. Kroeger, P.K. Hepler, P.W. Wiseman, A. Geitmann, Magnitude and direction of vesicle dynamics in growing pollen tubes using spatio-temporal image correlation spectroscopy and fluorescence recovery after photobleaching, Plant Physiol. 147 (2008) 1646–1658.
[29] P.W. Wiseman, C.M. Brown, D.J. Webb, B. Hebert, N.L. Johnson, J.A. Squier, M.H. Ellisman, A.F. Horwitz, Spatial mapping of integrin interactions and dynamics during cell migration by image correlation microscopy, J. Cell Sci. 117 (2004) 5521–5534.
[30] J.W. Comeau, D.L. Kolin, P.W. Wiseman, Accurate measurements of protein interactions in cells via improved spatial image cross-correlation spectroscopy, Mol. BioSyst. 4 (2008) 672–685.
[31] D.L. Kolin, P.W. Wiseman, Advances in image correlation spectroscopy: measuring number densities, aggregation states, and dynamics of fluorescently labeled macromolecules in cells, Cell Biochem. Biophys. 49 (2007) 141–164.
[32] A. Delon, Y. Usson, J. Derouard, T. Biben, C. Souchier, Photobleaching, mobility, and compartmentalisation: inferences in fluorescence correlation spectroscopy, J. Fluoresc. 14 (2004) 255–267.
[33] E.M.M. Manders, F.J. Verbeek, J.A. Aten, Measurement of co-localization of objects in dual-colour confocal images, J. Microsc. 169 (1993) 375–382.
[34] S. Bolte, F.P. Cordelières, A guided tour into subcellular colocalization analysis in light microscopy, J. Microsc. 224 (2006) 213–232.
[35] J.C. Crocker, D.G. Grier, Methods of digital video microscopy for colloidal studies, J. Colloid Interface Sci. 179 (1996) 298–310.
[36] T. Schmidt, G.J. Schutz, W. Baumgartner, H.J. Gruber, H. Schindler, Imaging of single molecule diffusion, Proc. Natl. Acad. Sci. U. S. A. 93 (1996) 2926–2929.
[37] K. Notelaers, S. Rocha, R. Paesen, N. Smisdom, B. De Clercq, J.C. Meier, J.M. Rigo, J. Hofkens, M. Ameloot, Analysis of alpha3 GlyR single particle tracking in the cell membrane, Biochim. Biophys. Acta 1843 (2014) 544–553.
[38] M. Wang, N.O. Petersen, Lipid-coated gold nanoparticles promote lamellar body formation in A549 cells, Biochim. Biophys. Acta Mol. Cell Biol. Lipids 1831 (2013) 1089–1097.
[39] M. Coue, S.L. Brenner, I. Spector, E.D. Korn, Inhibition of actin polymerization by latrunculin A, FEBS Lett. 213 (1987) 316–318.
[40] R. Mallik, D. Petrov, S.A. Lex, S.J. King, S.P. Gross, Building complexity: an in vitro study of cytoplasmic dynein with in vivo implications, Curr. Biol. 15 (2005) 2075–2085.
[41] X. Jiang, C. Rocker, M. Hafner, S. Brandholt, R.M. Dorlich, G.U. Nienhaus, Endo- and exocytosis of zwitterionic quantum dot nanoparticles by live HeLa cells, ACS Nano 4 (2010) 6787–6797.
[42] X. Nan, P.A. Sims, P. Chen, X.S. Xie, Observation of individual microtubule motor steps in living cells with endocytosed quantum dots, J. Phys. Chem. B 109 (2005) 24220–24224.
[43] M.J. Saxton, Single-particle tracking: the distribution of diffusion coefficients, Biophys. J. 72 (1997) 1744–1753.
[44] Y. Gambin, R. Lopez-Esparza, M. Reffay, E. Sierecki, N.S. Gov, M. Genest, R.S. Hodges, W. Urbach, Lateral mobility of proteins in liquid membranes revisited, Proc. Natl. Acad. Sci. U. S. A. 103 (2006) 2098–2102.
[45] P.G. Saffman, M. Delbruck, Brownian motion in biological membranes, Proc. Natl. Acad. Sci. U. S. A. 72 (1975) 3111–3113.
[46] A. Einstein, Über die von der molekularkinetischen Theorie der Wärme geforderte Bewegung von in ruhenden Flüssigkeiten suspendierten Teilchen, Ann. Phys. 322 (1905) 549–560.
[47] A.L. Zajac, Y.E. Goldman, E.L. Holzbaur, E.M. Ostap, Local cytoskeletal and organelle interactions impact molecular-motor-driven early endosomal trafficking, Curr. Biol. 23 (2013) 1173–1180.
[48] K.M. Trybus, Intracellular transport: the causes for pauses, Curr. Biol. 23 (2013) R623–R625.
[49] M.C. Beckerle, Microinjected fluorescent polystyrene beads exhibit saltatory motion in tissue culture cells, J. Cell Biol. 98 (1984) 2126–2132.
[50] N. Hirokawa, Kinesin and dynein superfamily proteins and the mechanism of organelle transport, Science (New York, N.Y.) 279 (1998) 519–526.
[51] T.D. Pollard, J.A. Cooper, Actin, a central player in cell shape and movement, Science (New York, N.Y.) 326 (2009) 1208–1212.
[52] H. Chen, J. Yang, P.S. Low, J.-X. Cheng, Cholesterol level regulates endosome motility via rab proteins, Biophys. J. 94 (2008) 1508–1520.
[53] S. Gasman, Y. Kalaidzidis, M. Zerial, RhoD regulates endosome dynamics through Diaphanous-related Formin and Src tyrosine kinase, Nat. Cell Biol. 5 (2003) 195–204.
[54] M. Esner, F. Meyenhofer, M. Kuhn, M. Thomas, Y. Kalaidzidis, M. Bickle, Development of a kinetic assay for late endosome movement, J. Biomol. Screen. 19 (7) (2014) 1070–1078.
[55] D. Bandyopadhyay, A. Cyphersmith, J.A. Zapata, Y.J. Kim, C.K. Payne, Lysosome transport as a function of lysosome diameter, PLoS One 9 (2014) e86847.
[56] C.J. Szymanski, W.H.t. Humphries, C.K. Payne, Single particle tracking as a method to resolve differences in highly colocalized proteins, Analyst 136 (2011) 3527–3533.
[57] S. Balint, I. Verdeny Vilanova, A. Sandoval Alvarez, M. Lakadamyali, Correlative live-cell and superresolution microscopy reveals cargo transport dynamics at microtubule intersections, Proc. Natl. Acad. Sci. U. S. A. 110 (2013) 3375–3380.